PHYSICAL REVIEW D **95,** 073002 (2017)

Better Higgs boson measurements through information geometry

Johann Brehmer,[1] Kyle Cranmer,[2] Felix Kling,[3] and Tilman Plehn[1]
[1]*Institut für Theoretische Physik, Universität Heidelberg, ITP Heidelberg 69120, Germany*
[2]*Center for Cosmology & Particle Physics, New York University, New York, New York 10003, USA*
[3]*University of California, Irvine, California 92697, USA*
(Received 20 January 2017; published 5 April 2017)

Information geometry can be used to understand and optimize Higgs boson measurements at the LHC. The Fisher information encodes the maximum sensitivity of observables to model parameters for a given experiment. Applied to higher-dimensional operators, it defines the new physics reach of any LHC signature. We calculate the Fisher information for Higgs production in weak boson fusion with decays into tau pairs and four leptons and for Higgs production in association with a single top quark. In a next step, we analyze how the differential information is distributed over phase space, which defines optimal event selections. Conversely, we consider the information in the distribution of a subset of the kinematic variables, showing which production and decay observables are the most powerful and how much information is lost in traditional histogram-based analysis methods compared to fully multivariate ones.

DOI: 10.1103/PhysRevD.95.073002

I. INTRODUCTION

Since its experimental discovery [1,2], the Higgs boson and its properties have quickly become one of the most important and active fields of research for physics beyond the Standard Model at the LHC. In the Lagrangian language of fundamental physics, the Higgs properties can be described by a continuous and high-dimensional parameter space, for example, in terms of Wilson coefficients in an effective field theory (EFT) [3–5]. One of the main features of moving from simple coupling modifications to higher-dimensional operators is that we can now include kinematic distributions in these searches [6,7]. A common challenge of all Higgs analyses is how to navigate the vast family of phase-space distributions.

Responding to the overwhelming number of search strategies, we expect the LHC Collaborations to focus more and more on high-level statistical tools, including hypothesis tests based on multivariate analysis with machine learning or the matrix element method [8,9]. Historically, these tools compare two discrete hypotheses, and applying them to continuous, high-dimensional parameter spaces is computationally expensive. Recently, machine learning techniques have been extended to include inference on such continuous high-dimensional parameter spaces [10]. With these capabilities, it becomes increasingly important to be able to effectively characterize the information contained in these distributions. We present an approach based on information geometry [11], intrinsically designed to study continuous parameter spaces of arbitrary dimensionality without the need for any discretization of the hypothesis. We use this to compare and improve Higgs measurement strategies.

Our central object is the Fisher information matrix. Through the Cramér-Rao bound, it determines the maximum knowledge on model parameters that we can derive from an observation [12,13]. In that sense, the Cramér-Rao bound for the Fisher information plays a similar role as the Neyman-Pearson lemma [14] plays for a discrete hypothesis test and the log-likelihood ratio: it allows us to define and to compute the best possible outcome of any multivariate black-box analysis [9,15]. In addition, the Fisher information matrix defines a metric in the space of model parameters, which not only provides an intuitive geometric picture, but also gives us a handle on the linearization of the observable in terms of new physics effects.

When we apply our information geometry framework to Higgs physics, in particular to analyses of the dimension-six Higgs Lagrangian, we can tackle the following types of questions:

(i) What is the maximum precision with which we can measure continuous model parameters?
(ii) How is the information distributed over phase space?
(iii) How much of the full information is contained in a given set of distributions?
(iv) Which role do higher-dimensional corrections in the EFT expansion play?

We demonstrate our approach using three examples: Higgs production in weak boson fusion (WBF) [16] with its tagging-jet kinematics [17] is well known to probe many aspects of the Higgs-gauge coupling structure [18]. Focusing on the WBF production kinematics, we first analyze its combination with a Higgs decay to tau leptons [19]. This will, for example, allow us to estimate how much of the entire information on higher-dimensional operators is typically included in the leading tagging jet distributions. Combining WBF production with a Higgs decay to ZZ^* pairs, we can test how much additional information is included in the decay distributions. Conceptually, this contrasts two ways to constrain the same effective

Lagrangian via large momentum flow through the relevant vertices or via precision observables [6]. Finally, we will test how useful Higgs production in association with a single top [20] is for a dimension-six operator analysis.

In a set of appendixes, we give a worked-out simple example for our approach, explain how we compute the Fisher information, show more information on our example processes, indicate how systematic or theory uncertainties can be included, and discuss the relation of our approach to standard log-likelihood ratios.

II. INFORMATION GEOMETRY AND CRAMÉR-RAO BOUND

At the LHC, we typically use a set of possibly correlated event rates $\mathbf{x}$ to measure a set of model parameters. Those can, for example, be a vector of Higgs couplings with the unknown true value $\mathbf{g}$. These Higgs couplings define a continuous, high-dimensional model space. The outcome of the measurement is an estimator for the couplings $\hat{\mathbf{g}}$ that follows a probability distribution $f(\hat{\mathbf{g}}|\mathbf{g})$. For an unbiased estimator, its expectation value is equal to its true value,

$$\bar{g}_i \equiv E[\hat{g}_i|\mathbf{g}] = g_i. \tag{1}$$

Our argument can be trivially extended to biased estimators. The variance, or for more than one model parameter, the covariance matrix,

$$C_{ij}(\mathbf{g}) \equiv E[(\hat{g}_i - \bar{g}_i)(\hat{g}_j - \bar{g}_j)|\mathbf{g}], \tag{2}$$

provides a measure of the precision of the measurement. For a set of uncorrelated measurements, the covariance matrix is a diagonal matrix made of the individual variances.

The relation $f(\mathbf{x}|\mathbf{g})$ between the measurement $\mathbf{x}$ and assumed true parameters $\mathbf{g}$ can be extracted from Monte Carlo and detector simulations. If we know it, we can describe the reach of a measurement using the Fisher information matrix:

$$I_{ij}(\mathbf{g}) \equiv -E\left[\frac{\partial^2 \log f(\mathbf{x}|\mathbf{g})}{\partial g_i \partial g_j}\middle|\mathbf{g}\right]. \tag{3}$$

The Cramér-Rao bound [12] states that the covariance matrix in Eq. (2) is bounded from below by the inverse Fisher information: the smallest achievable uncertainty is then given by

$$C_{ij} \geq (I^{-1})_{ij}. \tag{4}$$

Large entries in the Fisher information indicate directions in model space which can be measured well. Eigenvectors with eigenvalue zero are blind directions. Fortunately, the Fisher information is invariant under a reparametrization of the observables $\mathbf{x}$ and transforms covariantly under a reparametrization of the model parameters $\mathbf{g}$.

After removing blind directions, the Fisher information is a symmetric and positive definite rank-two tensor and defines a Riemannian metric on the model space [11]. This allows us to define a local as well as global distance measure in model space,

$$d_{\text{local}}(\mathbf{g}_b;\mathbf{g}_a) = \sqrt{(\mathbf{g}_a - \mathbf{g}_b)_i I_{ij}(\mathbf{g}_a)(\mathbf{g}_a - \mathbf{g}_b)_j}$$
$$d(\mathbf{g}_b,\mathbf{g}_a) = \min_{\mathbf{g}(s)} \int_{s_a}^{s_b} ds \sqrt{\frac{dg_i(s)}{ds} I_{ij}(\mathbf{g}(s)) \frac{dg_j(s)}{ds}}, \tag{5}$$

where the global distance is the length of a geodesic (the curve that minimizes the distance). Contours of constant distances define optimal error ellipsoids. The distance tracks how (un)likely it is to measure $\hat{\mathbf{g}} = \mathbf{g}_b$ given the true value $\mathbf{g} = \mathbf{g}_a$. If the estimator is distributed according to a multivariate Gaussian around the true value, the local distance values directly correspond to the difference in $\hat{\mathbf{g}}$ and $\mathbf{g}_a$ measured in standard deviations.

A typical LHC measurement includes an observed total number of events n, distributed over possible phase space positions $\mathbf{x}$. The probability distribution in Eq. (3) factorizes [9,15]

$$f(\mathbf{x}_1,\ldots,\mathbf{x}_n|\mathbf{g}) = \text{Pois}(n|L\sigma(\mathbf{g})) \prod_{i=1}^{n} f^{(1)}(\mathbf{x}_i|\mathbf{g}), \tag{6}$$

where $f^{(1)}(\mathbf{x}|\mathbf{g})$ is the normalized probability distribution for a single event populating the phase space position $\mathbf{x}$. This can be calculated, for example, with Monte Carlo simulations. The total cross section is $\sigma(\mathbf{g})$, to be multiplied with the integrated luminosity L. The corresponding Fisher information is

$$I_{ij} = \frac{L}{\sigma}\frac{\partial\sigma}{\partial g_i}\frac{\partial\sigma}{\partial g_j} - L\sigma E\left[\frac{\partial^2 \log f^{(1)}(\mathbf{x}|\mathbf{g})}{\partial g_i \partial g_j}\right]. \tag{7}$$

The Fisher information is additive when we combine phase-space regions. After integrating over the entire phase space, this full Fisher information defines the minimum covariance matrix possible.

Instead of integrating over the entire phase space, it is enlightening to study how the information is distributed in phase space. Consider the differential quantity $dI_{ij}/d\mathbf{v}$, where $\mathbf{v}$ is a kinematic variable like an invariant mass or angle calculated from $\mathbf{x}$. Here I_{ij} uses all the information in $\mathbf{x}$, but we are able to study the distribution of the information with respect to $\mathbf{v}$.[1] Such a distribution defines the important phase-space region for a measurement and should drive the design of event selections: it allows us to

[1]This is similar to how the log-likelihood ratio was studied differentially with MadMax [15,21].

calculate the information loss from kinematic cuts and to quantify the trade-off between signal purity and maximal information. Integrating over this differential information will reproduce the total Fisher information I_{ij}.

Conversely, if in Eq. (7) we replace the full phase space point $\mathbf{x}$ with a lower-dimensional set of kinematic variables $\mathbf{v}$, we will arrive at the information in this reduced set of kinematic variables. We refer to this as the information in distributions, and we will use this definition to identify how efficient analyses in terms of a small number of available kinematic distributions can be.

For our analysis, we parametrize the Higgs properties in terms of dimension-six operators [3–5],

$$\mathcal{L} = \mathcal{L}_{\rm SM} + \frac{f_i}{\Lambda^2}\mathcal{O}_i \quad \text{implying} \quad g_i = \frac{f_i v^2}{\Lambda^2}, \tag{8}$$

where the additional factor v^2 ensures that our parameters $\mathbf{g}$ are dimensionless, and the Standard Model corresponds to $\mathbf{g} = \mathbf{0}$. In Eq. (A8), we see that the Fisher information around this point, $I_{ij}(\mathbf{0})$, only measures the linear terms in $\mathbf{g} \propto 1/\Lambda^2$ and is not sensitive to higher corrections. Dimension-six squared contributions appear away from the Standard Model point and in the corresponding global distances. The difference between local and global distances, thus, provides a measure of the impact of $1/\Lambda^4$ contributions [22].

III. WEAK-BOSON-FUSION HIGGS TO TAUS

The first question we tackle with our information geometry approach is what we can learn about higher-dimensional operators from the nontrivial kinematics of weak-boson-fusion production. As a decay, we include a simple fermionic two-body decay $H \to \tau\tau$ [19]; see Fig. 1. For our proof of concept, we stick to a parton-level analysis at leading order. The dominant irreducible backgrounds are QCD Zjj production and electroweak Zjj production, both with the decay $Z \to \tau\tau$, and Higgs production in gluon fusion with $H \to \tau\tau$.

We do not simulate tau decays, but multiply the rates with the branching ratios for the semi-leptonic di-tau mode and assume the di-tau system can be reconstructed with the collinear approximation with a realistic resolution for $m_{\tau\tau}$. Following the procedure outlined in Refs. [15,21], we smear the $m_{\tau\tau}$ distributions using a Gaussian (with width 17 GeV) for Higgs production and a double Gaussian (where the dominant component has a width of 13 GeV) for Z production, estimated from Fig. 1(a) of Ref. [23]. The double Gaussian ensures an accurate description of the high-mass tail of the Z peak around $m_{\tau\tau} = m_H$. Otherwise, no detector effects are included. We require loose cuts,

$$\begin{aligned} p_{T,j} &> 20\ \text{GeV} \qquad |\eta_j| < 5.0 \qquad \Delta\eta_{jj} > 2.0 \\ p_{T,\tau} &> 10\ \text{GeV} \qquad |\eta_\tau| < 2.5, \end{aligned} \tag{9}$$

to include as much of phase space as possible.

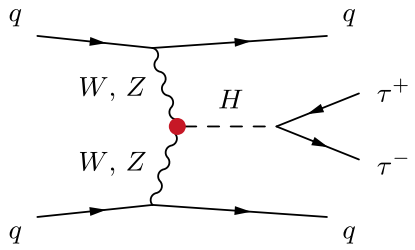

FIG. 1. Example Feynman diagram for weak-boson-fusion Higgs production with $H \to \tau\tau$. The red dot shows the Higgs-gauge interactions affected by the dimension-six operators of our analysis.

The different QCD radiation patterns of electroweak and QCD signal and background processes are a key feature to separate the signal from the background [17]. We take it into account through approximate individual jet veto survival probabilities [19],

$$\begin{aligned} \varepsilon^{\rm CJV}_{{\rm WBF}\,H} &= 0.71 \qquad \varepsilon^{\rm CJV}_{{\rm EW}\,Z} = 0.48 \\ \varepsilon^{\rm CJV}_{{\rm QCD}\,Z} &= 0.14 \qquad \varepsilon^{\rm CJV}_{{\rm GF}\,H} = 0.14. \end{aligned} \tag{10}$$

Since our phase space $\mathbf{x}$ does not include any jets other than the two tagging jets, we are not sensitive to details of the central jet veto other than the relative survival probabilities and possible second-order effects that would correlate the veto with $\mathbf{x}$. After the event selection of Eq. (9) and applying the CJV efficiencies, the WBF Higgs signal of 53 fb in the SM faces a dominant QCD Z background of 2.7 pb.

We consider five CP-even dimension-six operators in the HISZ basis [6,24],

$$\begin{aligned} \mathcal{O}_B &= i\frac{g}{2}(D^\mu\phi^\dagger)(D^\nu\phi)B_{\mu\nu} \qquad \mathcal{O}_W = i\frac{g}{2}(D^\mu\phi)^\dagger\sigma^k(D^\nu\phi)W^k_{\mu\nu} \\ \mathcal{O}_{BB} &= -\frac{g'^2}{4}(\phi^\dagger\phi)B_{\mu\nu}B^{\mu\nu} \qquad \mathcal{O}_{WW} = -\frac{g^2}{4}(\phi^\dagger\phi)W^k_{\mu\nu}W^{\mu\nu k} \\ \mathcal{O}_{\phi,2} &= \frac{1}{2}\partial^\mu(\phi^\dagger\phi)\partial_\mu(\phi^\dagger\phi). \end{aligned} \tag{11}$$

The first four operators introduce new Lorentz structures into Higgs-gauge interactions, which translate into changed kinematic shapes. The pure Higgs operator $\mathcal{O}_{\phi,2}$ leads to a universal rescaling of all single-Higgs couplings and otherwise only affects the Higgs self-coupling. Other operators that contribute to WBF Higgs production are tightly constrained by electroweak precision data or can be removed from the basis using field redefinitions [25]. The effect of $\mathcal{O}_{\phi,2}$ on gluon-fusion Higgs production is taken into account in our analysis, while the effects from $\mathcal{O}_W$ and $\mathcal{O}_B$ on the subleading electroweak Zjj background are neglected.

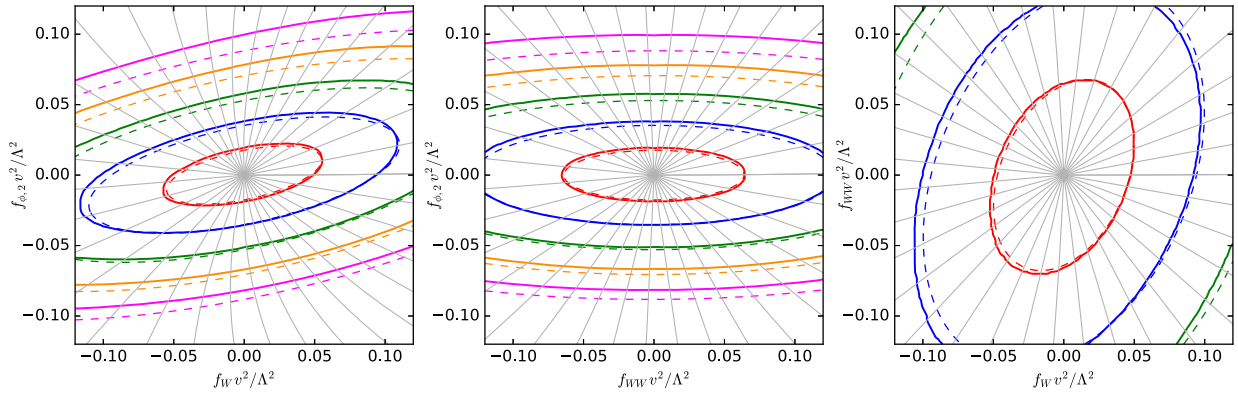

FIG. 2. Error ellipses defined by the Fisher information in the WBF $H \to \tau\tau$ channel. We show contours of local distance $d_{\text{local}}(\mathbf{g};\mathbf{0})$ (dashed) and global distance $d(\mathbf{g},\mathbf{0})$ (solid). The colored contours indicate distances of $d = 1...5$. In grey we show example geodesics. The g_i not shown are set to zero.

A. Maximum precision on Wilson coefficients

Following Eq. (8), our model space is spanned by five dimensionless parameters,

$$\mathbf{g} = \frac{v^2}{\Lambda^2}\begin{pmatrix} f_{\phi,2} \\ f_W \\ f_{WW} \\ f_B \\ f_{BB} \end{pmatrix}. \tag{12}$$

With these basis vectors, we calculate the Fisher information for 13 TeV using a combination of MadGraph5 [26], MadMax [21], and our own MadFisher algorithm, described in Appendix A 2. We absorb all particle identification and trigger efficiencies into a single universal ε (which does not include the process-dependent CJV efficiencies). Then, for our toy example, we assume the integrated luminosity times universal efficiencies to be $L \cdot \varepsilon = 30\ \text{fb}^{-1}$. We find

$$I_{ij}(\mathbf{0}) = \begin{pmatrix} 3202.1 & -625.3 & -7.2 & -34.8 & 0.3 \\ -625.3 & 451.0 & -109.5 & 23.3 & -1.5 \\ -7.2 & -109.5 & 243.7 & -5.5 & 2.8 \\ -34.8 & 23.3 & -5.5 & 4.1 & -0.3 \\ 0.3 & -1.5 & 2.8 & -0.3 & 0.1 \end{pmatrix}. \tag{13}$$

The eigenvectors, ordered by the size of their eigenvalues, are

$$\mathbf{g}_1 = \begin{pmatrix} 0.98 \\ -0.21 \\ 0.01 \\ -0.01 \\ 0.00 \end{pmatrix} \quad \mathbf{g}_2 = \begin{pmatrix} -0.18 \\ -0.79 \\ 0.58 \\ -0.04 \\ 0.01 \end{pmatrix} \quad \mathbf{g}_3 = \begin{pmatrix} 0.12 \\ 0.57 \\ 0.81 \\ 0.03 \\ 0.01 \end{pmatrix} \quad \mathbf{g}_4 = \begin{pmatrix} 0.00 \\ -0.05 \\ 0.00 \\ 1.00 \\ -0.07 \end{pmatrix} \quad \mathbf{g}_5 = \begin{pmatrix} 0.00 \\ -0.00 \\ -0.01 \\ 0.07 \\ 1.00 \end{pmatrix}. \tag{14}$$

The corresponding eigenvalues are (3338,395,165,2.9,0.1), indicating that the WBF process has very different sensitivities to the five operators: $\mathcal{O}_{\phi,2}$ can be most strongly constrained and is weakly correlated with $\mathcal{O}_W$. It is followed by the strongly correlated $\mathcal{O}_W - \mathcal{O}_{WW}$ plane. The sensitivity to $\mathcal{O}_B$ and $\mathcal{O}_{BB}$, which only play a role in subleading Z-mediated production diagrams, is much smaller and shows very little correlation with each other and everything else.

We visualize our results as contours of the local and global distances defined in Eq. (5) for slices of parameter space in Fig. 2. First, the contours show the maximum precision that can be attained in a measurement in this process. Without taking into account systematic uncertainties, an optimal measurement will probe the $\mathcal{O}_{\phi,2}$ direction with $\Delta g \approx 0.02$, translating into $\Lambda/\sqrt{f_{\phi,2}} \approx 1.8$ TeV. The $\mathcal{O}_W$ and $\mathcal{O}_{WW}$ directions can optimally be probed at the $\Delta g \approx 0.05$ or $\Lambda/\sqrt{f_{\phi,2}} \approx 1.1$ TeV level.

Comparing the local and global distances provides some insight into the role of $\mathcal{O}(1/\Lambda^4)$ effects, as discussed before. At $d = 1$, 2 the differences are small, signaling that an optimal measurement will be dominated by the linearized dimension-six amplitudes. On the other hand,

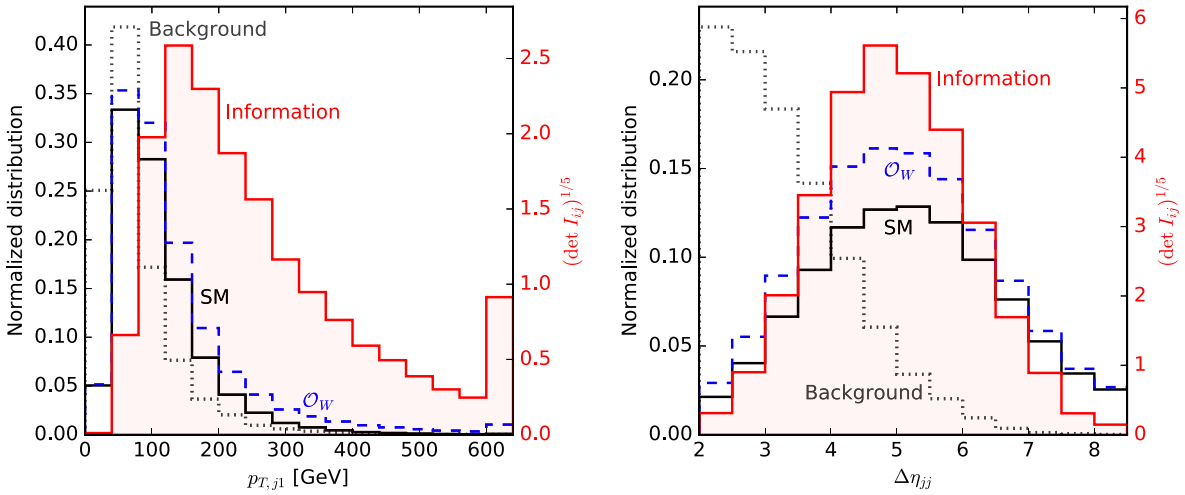

FIG. 3. Distribution of the Fisher information in the WBF $H \to \tau\tau$ channel (shaded red). We also show the normalized SM signal (solid black) and QCD Z + jets (dotted grey) rates. The dashed blue line shows the effect of an exaggerated $f_W v^2/\Lambda^2 = 0.5$. The last bin is an overflow bin.

analyses based on less luminosity or requiring more stringent exclusion criteria (translating into larger distances) will only probe new physics scales closer to the electroweak scale, in which case the squared dimension-six terms will have a larger effect.

B. Differential information

The fact that the Fisher information is additive across different phase-space regions means that we can consider the differential information with respect to phase space ($dI_{ij}/d\mathbf{x}$) or a specific kinematic variable ($dI_{ij}/d\mathbf{v}$). In Fig. 3, we show the differential cross sections of the signal and dominant background process for typical kinematic distributions and compare it to the differential information. More distributions are shown in Appendix A 3.

Obviously, the signal-to-background ratio improves for large invariant masses of the tagging jets and towards $m_{\tau\tau}$ values around the Higgs mass. The information is larger in these phase-space regions, independent of the direction in model space. On the other hand, most of our dimension-six operators include derivatives, leading to an increasing amplitude with momentum transfer through the gauge-Higgs vertex. This momentum flow is not observable, but the transverse momenta of the tagging jets and the Higgs boson are strongly correlated with it [22]. Indeed most of the information on higher-dimensional operators comes from the high-energy tail of p_{T,j_1}.

The rapidity difference between the tagging jets indicates a trade-off between these two effects: on the one hand, at larger rapidity distances the signal-to-background ratio clearly improves [18]. On the other hand, the largest effects from dimension-six operators appear at smaller $\Delta\eta_{jj}$, again driven by the larger momentum transfer [22]. In the right panel of Fig. 3, we see that the information on these operators comes from $\Delta\eta_{jj} = 3\ldots7$. Tight cuts with the aim to remove backgrounds lose a sizable fraction of the information on dimension-six operators.

C. Information in distributions

While the integrated, fully differential information defined in Eq. (7) provides us with optimal experimental results, it remains to be shown that we can access it in practice. Recent proposals using machine learning for high-dimensional likelihood fits aim to tackle exactly this problem [10]. Regardless, a relevant question is how much of this maximum information is retained in simple one-dimensional or two-dimensional distributions of standard kinematic observables $\mathbf{v}$.

In the presence of backgrounds, a histogram-based analysis first requires a stringent event selection, either based on traditional kinematic cuts or on a multivariate classifier. First, we choose the WBF cuts:

$$105\ \text{GeV} < m_{\tau\tau} < 165\ \text{GeV} \qquad p_{T,j_1} > 50\ \text{GeV}$$
$$m_{jj} > 1\ \text{TeV} \qquad \Delta\eta_{jj} > 3.6. \tag{15}$$

This improves the signal-to-background ratio to approximately unity, but at the cost of losing discrimination power. Eventually, a histogram-based analysis will benefit from optimizing this selection, for instance foregoing the simple cuts for a multivariate approach, going beyond the scope of this demonstration. Based on this selection, we analyze the distributions:

(i) p_{T,τ_1} with bin size 25 GeV up to 500 GeV and an overflow bin;
(ii) $m_{\tau\tau}$ with bin size 5 GeV in the allowed range of 105...165 GeV;
(iii) $p_{T,\tau\tau}$ with bin size 50 GeV up to 800 GeV and an overflow bin;

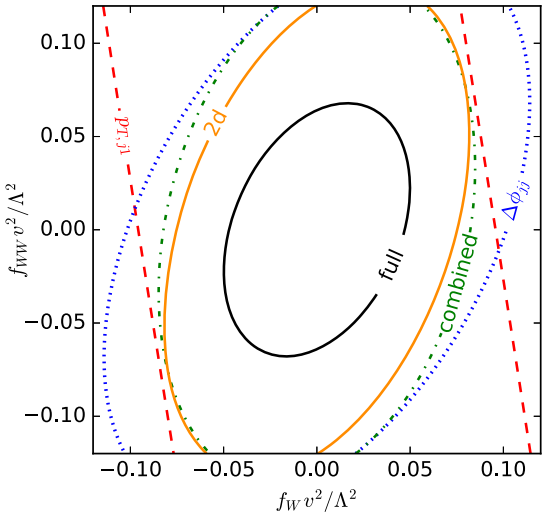

FIG. 4. Information from histograms compared to the full information (black) in the WBF $H \to \tau\tau$ channel, shown as contours $d_{\text{local}}(\mathbf{g};\mathbf{0}) = 1$. We include p_{T,j_1}, $\Delta\phi_{jj}$, their naive combination assuming no mutual information, and their two-dimensional histogram. The g_i not shown are set to zero.

(iv) p_{T,j_1} with bin size 50 GeV up to 800 GeV and an overflow bin;
(v) m_{jj} with bin size 250 GeV up to 4 TeV and an overflow bin;
(vi) $\Delta\eta_{jj}$ with bin size 0.5 up to 8.0 and an overflow bin;
(vii) $\Delta\phi_{jj} = \phi_{j_{\eta<0}} - \phi_{j_{\eta>0}}$ [27] with bin size $2\pi/20$;
(viii) $\Delta\eta_{\tau\tau,j1}$ with bin size 0.5 up to 8.0 and an overflow bin;
(ix) $\Delta\phi_{\tau\tau,j1}$ with bin size $\pi/10$.

Figure 4 demonstrates that virtuality measures, such as the transverse momentum of the leading tagging jet, mostly constrain $\mathcal{O}_W$, while angular correlations between the jets are more sensitive to $\mathcal{O}_{WW}$. Stringent constraints on the full operator space can only be achieved by combining the information in these (or more) distributions, ideally in a two-dimensional histogram.

In Fig. 5, we extend our comparison to the information in all of the above distributions. The top panel shows the eigenvalues of the individual information matrices, and the colors indicate which operators the corresponding eigenvectors are composed of. This allows us to see which operators can be measured well in which distributions, and where blind (or flat) directions arise. In the lower panel, we compare the determinants, providing a straightforward measure of the information in distributions that is invariant under basis rotations.

In general, single differential cross sections probe individual directions in phase space well, but always suffer from basically blind directions. To maximize the constraining power on all operators, we need to combine virtuality measures and angular correlations. Even then, there is a substantial difference to the maximum information in the process: the combined analysis of jet transverse

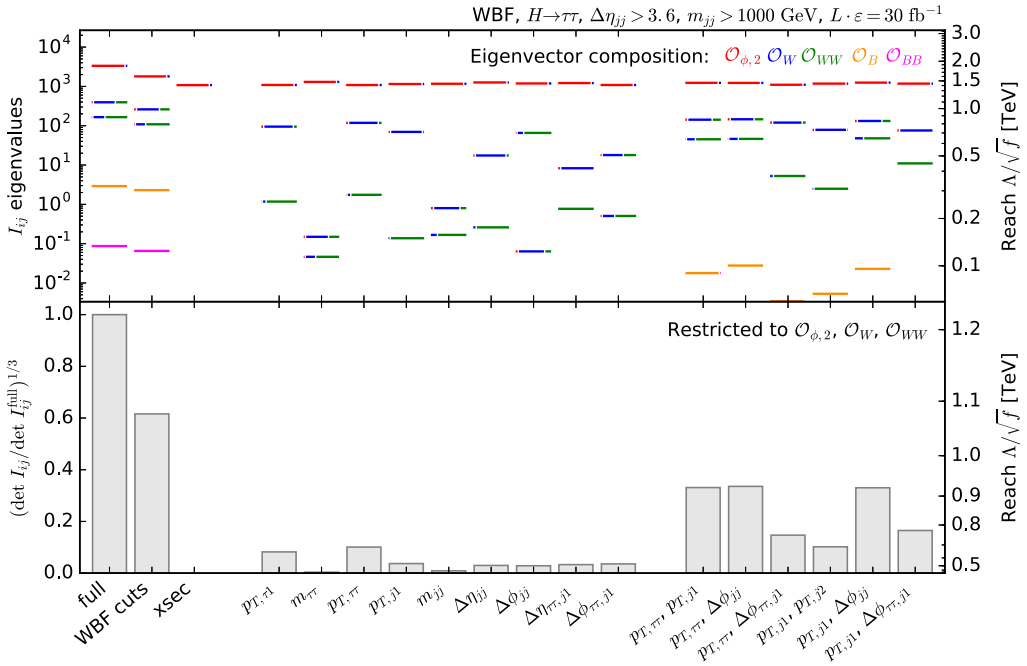

FIG. 5. Fisher information for the WBF $H \to \tau\tau$ channel exploiting the full phase space, after the cuts in Eq. (15), and for several kinematic distributions. The top panel shows the eigenvalues, the colors denote the composition of the corresponding eigenvectors. The right axis translates the eigenvalues into a new physics reach for the corresponding combination of Wilson coefficients. In the bottom panel, we show the determinants of the Fisher information restricted to $\mathcal{O}_{\phi,2}$, $\mathcal{O}_W$, and $\mathcal{O}_{WW}$, normalized to the full information. Again, the right axis translates them into a new physics reach.

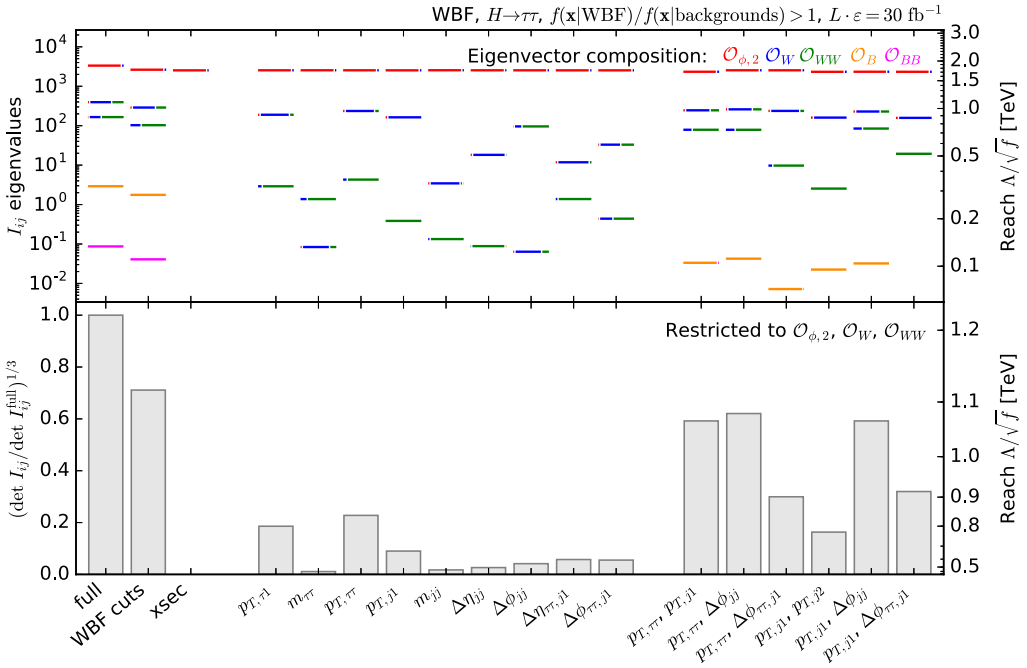

FIG. 6. Fisher information for the WBF $H \to \tau\tau$ channel exploiting the full phase space, after the likelihood-based event selection in Eq. (16), and for several kinematic distributions. Except for the initial cuts, the plot is analogous to Fig. 5.

momenta and $\Delta\phi_{jj}$ has a new physics reach in the $\mathcal{O}_{\phi,2} - \mathcal{O}_W - \mathcal{O}_{WW}$ space of 0.9 TeV, compared to 1.2 TeV for the fully differential cross section. Under our simplistic assumptions this corresponds to roughly 3 times more data. Half of this loss in constraining power is due to information in background-rich regions discarded by the WBF cuts, and half is due to nontrivial kinematics not captured by the double differential distributions.

In light of the large amount of information discarded by the WBF cuts in Eq. (15), we repeat this comparison with an alternative multivariate event selection. Instead of cutting on standard kinematic observables, we select all events in "signal-like" phase-space regions, defined as those with a larger expected SM WBF rate than expected background rates,

$$\frac{\sigma_{\text{SM WBF}} f^{(1)}(\mathbf{x}|\text{SM WBF})}{\sigma_{\text{backgrounds}} f^{(1)}(\mathbf{x}|\text{backgrounds})} = \frac{\Delta\sigma_{\text{SM WBF}}(\mathbf{x})}{\Delta\sigma_{\text{backgrounds}}(\mathbf{x})} > 1. \tag{16}$$

We then calculate the information in the same distributions as before.

As shown in Fig. 6, the cut in Eq. (16) defines a sample with little background contamination without sacrificing much discrimination power. One-dimensional and two-dimensional distributions can extract information on the operators more reliably than after the kinematic event selection in Eq. (15). A combined measurement of the jet transverse momenta and $\Delta\phi_{jj}$ is now able to probe new physics scales of up to 1.1 compared to 1.2 GeV for the fully multivariate approach, corresponding to 70% more data.

IV. WEAK-BOSON-FUSION HIGGS TO FOUR LEPTONS

Another question we can approach with information geometry is how much the nontrivial decay mode $H \to 4\ell$ adds to the WBF production analyzed in Sec. III. For this particularly clean channel, shown in Fig. 7, the backgrounds are not the limiting factor, so we omit them for our toy study. For instance, in the relevant phase-space region, the cross section of the dominant irreducible $ZZ^* jj$ background is over an order of magnitude smaller than the SM Higgs signal. This also allows us to avoid smearing the $m_{4\ell}$ distribution. At the parton level, we apply the generator-level cuts,

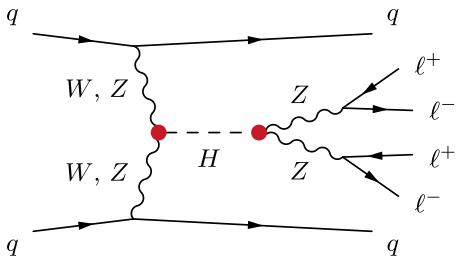

FIG. 7. Example Feynman diagram for weak-boson-fusion Higgs production with $H \to 4\ell$. The red dots show the Higgs-gauge interactions affected by the dimension-six operators of our analysis.

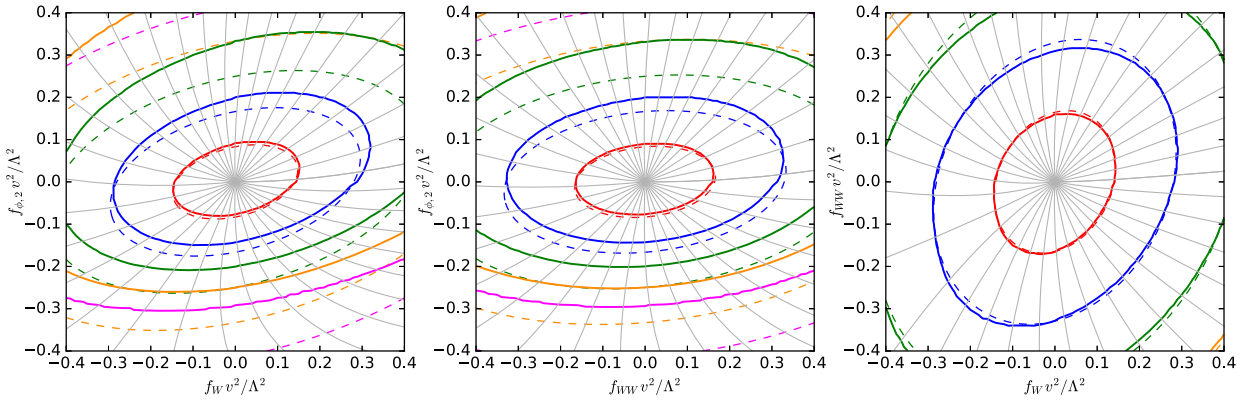

FIG. 8. Error ellipses defined by the Fisher information in the WBF $H \to 4\ell$ channel. We show contours of local distance $d_{\text{local}}(\mathbf{g};\mathbf{0})$ (dashed) and global distance $d(\mathbf{g},\mathbf{0})$ (solid). The colored contours indicate distances of $d = 1...5$. In grey we show example geodesics. The g_i not shown are set to zero.

$$\begin{aligned} p_{T,j} &> 20\ \text{GeV} \qquad |\eta_j| < 5.0 \\ p_{T,\ell} &> 10\ \text{GeV} \qquad |\eta_\ell| < 2.5, \end{aligned} \tag{17}$$

with $\ell = e,\ \mu$. The SM cross section after these cuts is 0.36 fb.

A. Maximum precision on Wilson coefficients

Again we study the five-dimensional space of CP-even Wilson coefficients given in Eq. (12). For increased luminosity, $L \cdot \varepsilon = 100\ \text{fb}^{-1}$, we find the SM information,

$$I_{ij}(\mathbf{0}) = \begin{pmatrix} 144.3 & -27.3 & -11.5 & -1.6 & -0.7 \\ -27.3 & 50.9 & -9.1 & 6.7 & -0.2 \\ -11.5 & -9.1 & 36.9 & -1.2 & 1.0 \\ -1.6 & 6.7 & -1.2 & 1.9 & -0.1 \\ -0.7 & -0.2 & 1.0 & -0.1 & 0.1 \end{pmatrix}, \tag{18}$$

with the eigenvectors

$$\mathbf{g}_1 = \begin{pmatrix} 0.96 \\ -0.25 \\ -0.08 \\ -0.02 \\ 0.00 \end{pmatrix} \quad \mathbf{g}_2 = \begin{pmatrix} -0.16 \\ -0.79 \\ 0.58 \\ -0.11 \\ 0.02 \end{pmatrix} \quad \mathbf{g}_3 = \begin{pmatrix} 0.21 \\ 0.54 \\ 0.81 \\ 0.09 \\ 0.02 \end{pmatrix}$$

$$\mathbf{g}_4 = \begin{pmatrix} 0.02 \\ 0.14 \\ 0.01 \\ -0.99 \\ 0.04 \end{pmatrix} \quad \mathbf{g}_5 = \begin{pmatrix} 0.00 \\ -0.00 \\ -0.03 \\ 0.04 \\ 1.00 \end{pmatrix} \tag{19}$$

and the eigenvalues (152.4,52.8,27.8,1.0,0.0).

The Fisher information approach allows us to directly compare this outcome to our earlier results for WBF production with $H \to \tau\tau$ in Eq. (13) or to calculate the combined information in these two channels by simply adding their Fisher information matrices after rescaling them to the same luminosity. Clearly, the $\tau\tau$ channel contains significantly more information on all operators. The decay $H \to 4\ell$ does not even increase the sensitivity to $\mathcal{O}_B$ or $\mathcal{O}_{BB}$; both of them are still basically blind directions. We visualize the information geometry in the remaining directions in Fig. 8. The differences between local and global distances are much larger than in the $H \to \tau\tau$ channel. This is because the tiny $H \to 4\ell$ branching fraction decreases the new physics reach and with it the hierarchy of scales in our effective Lagrangian. This means that the squared dimension-six amplitudes are numerically more relevant.

B. Production vs decay kinematics

Focusing on the question of how the decay analysis improves our global information, we disentangle the effects on the production and decay vertices in Fig. 9. As is well known for the LHC, the production-side analysis benefits from a large momentum flow through the Higgs vertex, while the momentum flow through the decay vertices is bounded by the Higgs mass (neglecting off-shell phase space regions). For momentum-dependent operators, this disadvantage is not compensated by the complex $H \to 4\ell$ decay kinematics. Consequently, the Higgs decay only improves the reach in the $\mathcal{O}_{\phi,2}$ direction, corresponding to a change in the total rate. This operator also affects many other total Higgs rates, so we conclude that the complex $H \to 4\ell$ kinematics does not play a significant role as part of a global analysis.

In complete analogy to Fig. 5 for the WBF production, we compare the information in different distributions for CP-even operators in Fig. 10. The standard tagging jet observables are complemented by five observables characterizing the 4ℓ decay kinematics,

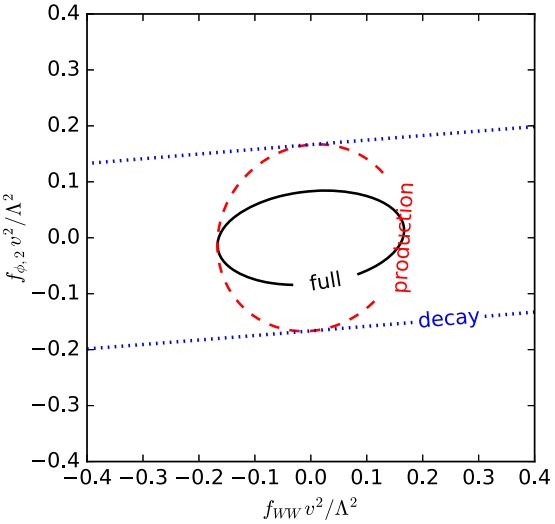

FIG. 9. Information in the WBF $H \to 4\ell$ channel from including dimension-six operators only in the production vertex (red), only in the decay vertex (blue), and in both (black). The information is visualized as local contours $d_{\text{local}}(\mathbf{g};\mathbf{0}) = 1$. The g_i not shown are set to zero.

(i) p_{T,ℓ_1};
(ii) $p_{T,4\ell}$;
(iii) m_{Z_2} for the lower-mass reconstructed Z boson;
(iv) $\cos\theta_1 = \hat{p}_{\ell_1^-} \cdot \hat{p}_{Z_2}|_{Z_1}$ defined in terms of unit-3-vectors $\hat{p}$, and analogously $\cos\theta_2$;
(v) $\cos\Phi = (\hat{p}_{\ell_1^-} \times \hat{p}_{\ell_1^+}) \cdot (\hat{p}_{\ell_2^-} \times \hat{p}_{\ell_2^+})$, defined in the ZZ or Higgs rest frame [18].

In all cases, we use at least ten bins and include underflow and overflow bins where applicable.

In our quantitative analysis, we find similar patterns as in the $\tau\tau$ mode. The key observables are again transverse momenta and jet angular correlations. Without the complication of removing backgrounds efficiently, the combined analysis of these variables comes close to the maximum information: a two-dimensional histogram of jet transverse momenta and $\Delta\phi_{jj}$ probes new physics scales up to 650 GeV, while for a fully differential analysis the maximum probed new physics scale is close to 700 GeV. Under our assumptions, this difference roughly corresponds to 25% more data. The decay kinematics and its angular observables do not help significantly or change the picture qualitatively. This shows again how much the sensitivity of the decay vertices to dimension-six operators is limited by the restriction of the momentum flow to the Higgs mass. This is not accidental: the reason behind this role of the momentum dependence is that for all operators shown in Eq. (12), with the exception of $\mathcal{O}_{\phi,2}$, gauge invariance forces us to include the field strength tensor instead of the gauge boson field, automatically introducing a momentum dependence.

V. HIGGS PLUS SINGLE TOP

Our final example is Higgs production with a single top with $H \to \gamma\gamma$ and a hadronic top decay. As shown in

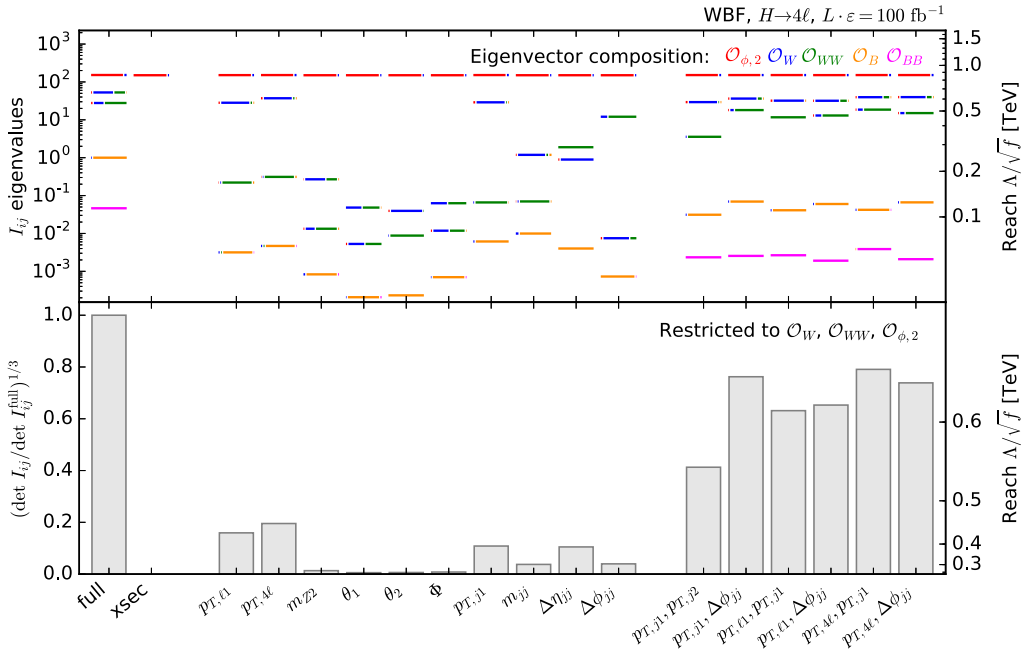

FIG. 10. Fisher information for the WBF $H \to 4\ell$ channel based on the full kinematics and on individual kinematic distributions. The top panel shows the eigenvalues, the colors denote the composition of the corresponding eigenvectors. The right axis translates the eigenvalues into a new physics reach for the corresponding combination of Wilson coefficients. In the bottom panel, we show the determinants of the Fisher information restricted to $\mathcal{O}_{\phi,2}$, $\mathcal{O}_W$, and $\mathcal{O}_{WW}$, normalized to the full information. Again, the right axis translates them into a new physics reach.

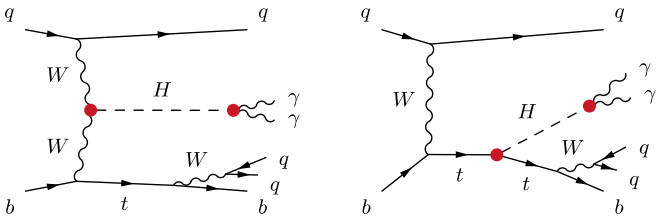

FIG. 11. Example Feynman diagrams for Higgs production with a single top, not resolving the loop-induced $H\gamma\gamma$ coupling. The red dots show the Higgs interactions affected by the dimension-six operators of our analysis.

Fig. 11, diagrams where the Higgs is radiated off a W boson interfere destructively with diagrams with a top-Higgs coupling, making this channel a direct probe of the sign of the top Yukawa coupling [20]. We stick to a parton-level analysis at leading order in the five-flavor scheme. For our toy example, we include only one of the dominant backgrounds, single top production with two photons, and, in particular, ignore the multijet background. The subleading $t\bar{t}\gamma\gamma$ background populates qualitatively different phase-space regions from the single-top signal and can be supressed with an appropriate event selection [28]. We smear the $m_{\gamma\gamma}$ distribution of the signal process with a Gaussian of width 1.52 GeV estimated from Fig. 6(b) of Ref. [29] and do not include any other detector effects. Our basic event selection requires

$$\begin{aligned} p_{T,j} &> 20\ \text{GeV} \qquad |\eta_j| < 5.0 \\ \Delta R_{jj} &> 0.4 \qquad 152\ \text{GeV} < m_{bjj} < 192\ \text{GeV} \\ p_{T,\gamma} &> 10\ \text{GeV} \qquad |\eta_\gamma| < 2.5 \\ \Delta R_{\gamma j}, \Delta R_{\gamma\gamma} &> 0.4 \qquad 120\ \text{GeV} < m_{\gamma\gamma} < 130\ \text{GeV}, \end{aligned} \tag{20}$$

leading to a SM tH cross section of 0.10 fb and a background of 0.22 fb.

We consider four CP-even dimension-six operators

$$\begin{aligned} \mathcal{O}_W &= i\frac{g}{2}(D^\mu\phi)^\dagger\sigma^k(D^\nu\phi)W^k_{\mu\nu} \\ \mathcal{O}_{t\phi} &= (\phi^\dagger\phi)(\bar{Q}_3\tilde{\phi}t_R) + \text{H.c.} \\ \mathcal{O}_{WW} &= -\frac{g^2}{4}(\phi^\dagger\phi)W^k_{\mu\nu}W^{\mu\nu k} \\ \mathcal{O}_{\phi,2} &= \frac{1}{2}\partial^\mu(\phi^\dagger\phi)\partial_\mu(\phi^\dagger\phi). \end{aligned} \tag{21}$$

The operators $\mathcal{O}_W$ and $\mathcal{O}_{WW}$ affect the production amplitudes where the Higgs couples to a W, while $\mathcal{O}_{t\phi}$ rescales the top Yukawa coupling. Both $\mathcal{O}_{WW}$ and $\mathcal{O}_{\phi,2}$ also affect the $H \to \gamma\gamma$ decay.

A. Maximum precision on Wilson coefficients

We calculate the Fisher information in terms of the dimensionless parameters,

$$\mathbf{g} = \frac{v^2}{\Lambda^2}\begin{pmatrix} f_{\phi,2} \\ f_W \\ f_{WW} \\ f_{t\phi} \end{pmatrix}, \tag{22}$$

for 13 TeV and an integrated luminosity times efficiencies of $L \cdot \varepsilon = 300\ \text{fb}^{-1}$ and find

$$I_{ij}(\mathbf{0}) = \begin{pmatrix} 80.1 & -18.7 & -957.0 & 13.2 \\ -18.7 & 32.6 & 221.7 & 27.0 \\ -957.0 & 221.7 & 11446.1 & -146.0 \\ 13.2 & 27.0 & -146.0 & 150.3 \end{pmatrix}. \tag{23}$$

The eigenvectors are

$$\mathbf{g}_1 = \begin{pmatrix} 0.08 \\ -0.02 \\ -1.00 \\ 0.01 \end{pmatrix} \quad \mathbf{g}_2 = \begin{pmatrix} 0.00 \\ -0.23 \\ -0.01 \\ -0.97 \end{pmatrix}$$
$$\mathbf{g}_3 = \begin{pmatrix} -0.02 \\ 0.97 \\ -0.02 \\ -0.23 \end{pmatrix} \quad \mathbf{g}_4 = \begin{pmatrix} 1.00 \\ 0.02 \\ 0.08 \\ -0.01 \end{pmatrix}, \tag{24}$$

with corresponding eigenvalues (11532,155,21.3,0.1). The best constrained direction is along $\mathcal{O}_{WW}$ and corresponds to the combination of Wilson coefficients that affects the $H \to \gamma\gamma$ decay in addition to production effects, which will already be tightly constrained once a tH measurement is feasible. The orthogonal direction in the $\mathcal{O}_{\phi,2} - \mathcal{O}_{WW}$ plane is for all practical purposes blind. Even with the assumed sizeable event rate corresponding to 300 fb^{-1}, the sensitivity to $\mathcal{O}_W$ and $\mathcal{O}_{t\phi}$ is limited, with some mixing between the two operators.

We visualize this maximum sensitivity to dimension-six operators in Fig. 12. With the exception of $\mathcal{O}_{WW}$, an optimal measurement can probe all operators at the $\Delta g \approx 0.1\ldots0.2$ level, equivalent to $\Lambda/\sqrt{f_{\phi,2}} \approx 600\ldots750$ GeV. There are large differences between local and global distances already at the $d = 2$ level, implying that a measurement of this channel will always be sensitive to the squared dimension-six terms.

B. Differential information

In Fig. 13, we show the distribution of this information over phase space. More distributions are shown in Appendix A 3. As expected, the information is concentrated in the $m_{\gamma\gamma} \sim m_H$ peak and in the high-energy tails of transverse momenta. Studying angular correlations between the Higgs system and the top decay products,

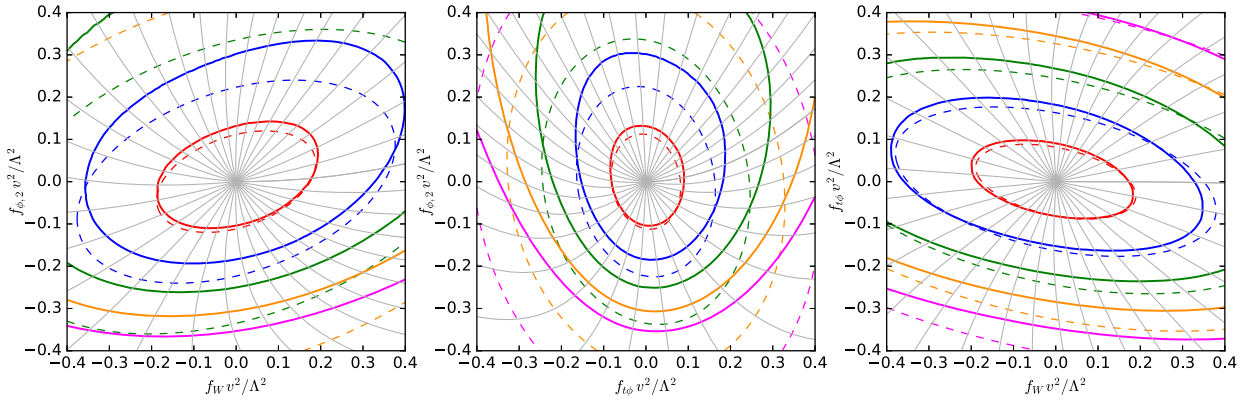

FIG. 12. Error ellipses defined by the Fisher information in Higgs plus single top production. We show contours of local distance $d_{\text{local}}(\mathbf{g};\mathbf{0})$ (dashed) and global distance $d(\mathbf{g},\mathbf{0})$ (solid). The colored contours indicate distances of $d = 1...5$. In grey we show example geodesics. The g_i not shown are set to zero.

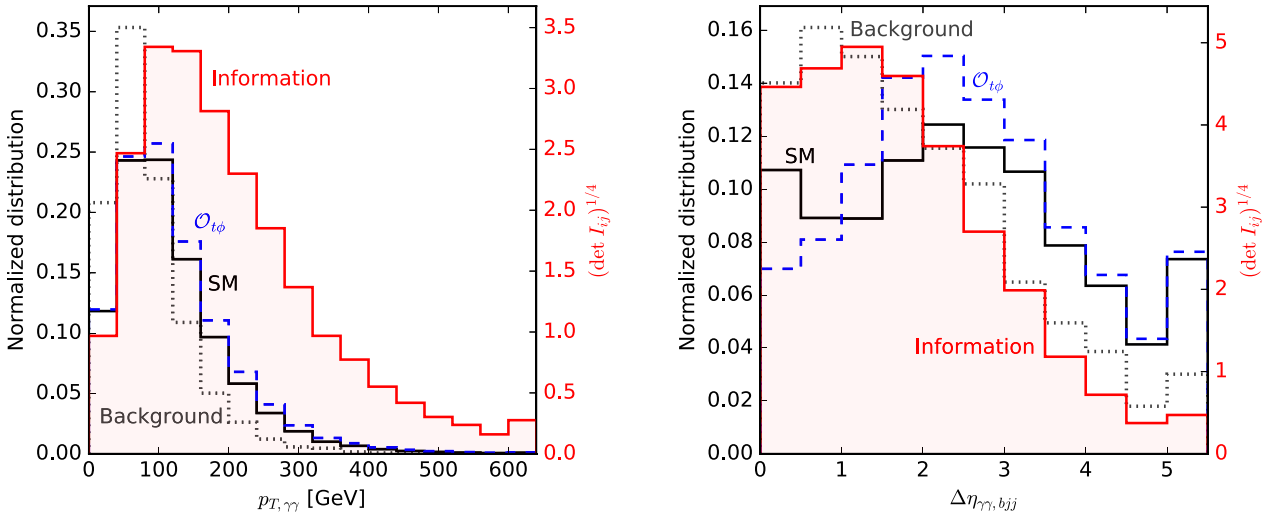

FIG. 13. Distribution of the Fisher information in the Higgs plus single top channel (shaded red). We also show the normalized SM signal (solid black) and single-top background (dotted grey) rates. The dashed blue line shows the effect of $f_{t\phi}v^2/\Lambda^2 = 0.2$. The last bin is an overflow bin.

we find that the region $\Delta\eta_{\gamma\gamma,bjj} \lesssim 3$ contains a lot of discrimination power.

C. Information in distributions

In a next step, we compare this full information to the reduced information in one-dimensional and two-dimensional distributions of kinematic observables. We now require harder cuts,

$$p_{T,j_1} > 50\ \text{GeV} \qquad p_{T,\gamma} > 50, 30\ \text{GeV}$$
$$122\ \text{GeV} < m_{\gamma\gamma} < 128\ \text{GeV}, \tag{25}$$

which reduces the background to the level of the signal. We then analyze the distributions [20,28]:

(i) p_{T,γ_1} with bin size 25 GeV up to 400 GeV and an overflow bin;
(ii) $m_{\gamma\gamma}$ with bin size 1 GeV in the allowed range of 123...127 GeV;
(iii) $p_{T,\gamma\gamma}$ with bin size 40 GeV up to 600 GeV and an overflow bin;
(iv) $\Delta\phi_{\gamma\gamma}$ with bin size $\pi/10$;
(v) p_{T,j_1} with bin size 40 GeV up to 400 GeV and an overflow bin;
(vi) $p_{T,b}$ with bin size 40 GeV up to 400 GeV and an overflow bin;
(vii) $p_{T,bjj}$ with bin size 40 GeV up to 600 GeV and an overflow bin;
(viii) $\Delta\phi_{\gamma\gamma,b}$ with bin size $\pi/10$;
(ix) $\Delta\eta_{\gamma\gamma,b}$ with bin size 0.5 up to 5.0 and an overflow bin;

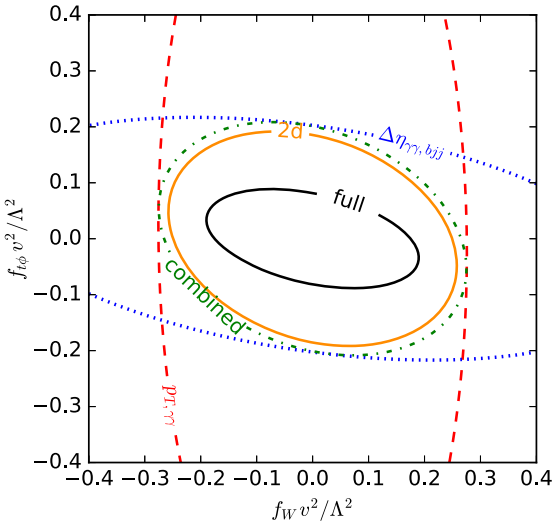

FIG. 14. Information from histograms compared to the full information (black), shown as contours $d_{\text{local}}(\mathbf{g};\mathbf{0}) = 1$. We include $p_{T,\gamma\gamma}$, $\Delta\eta_{\gamma\gamma,bjj}$, their naive combination assuming no mutual information, and their two-dimensional histogram. The g_i not shown are set to zero.

(x) $m_{\gamma\gamma bjj}$ with bin size 100 GeV up to 1500 GeV and an overflow bin;
(xi) $p_{T,\gamma\gamma bjj}$ with bin size 40 GeV up to 400 GeV and an overflow bin;
(xii) $\Delta\phi_{\gamma\gamma,bjj}$ with bin size $\pi/10$;
(xiii) $\Delta\eta_{\gamma\gamma,bjj}$ with bin size 0.5 up to 5.0 and an overflow bin.

As in the WBF case, different observables probe different Wilson operators. Figure 14 shows that the di-photon transverse momentum constrains mostly the $\mathcal{O}_W$ direction, while the rapidity separation between the Higgs and top systems is more sensitive to $\mathcal{O}_{t\phi}$.

In Fig. 15, we compare the eigenvalues, eigenvectors and determinants of the information matrices in all of the above distributions. We confirm that the photon observables mostly probe changes in the Higgs-gauge coupling from $\mathcal{O}_W$, while a rescaled top Yukawa will be visible in the properties of the top decay products. Distributions of the properties of the b jet consistently contain significantly less information than the corresponding distributions for the reconstructed top system. The rapidity difference between the $\gamma\gamma$ system and the reconstructed top provides a particularly good probe of this operator [20]. Combining this variable with the transverse momentum of the $\gamma\gamma$ system we can probe new physics scales in the $\mathcal{O}_{\phi,2} - \mathcal{O}_W - \mathcal{O}_{t\phi}$ space around 550 GeV, compared to 700 GeV for the fully differential cross section. This corresponds to almost 3 times more data under our simplifying assumptions.

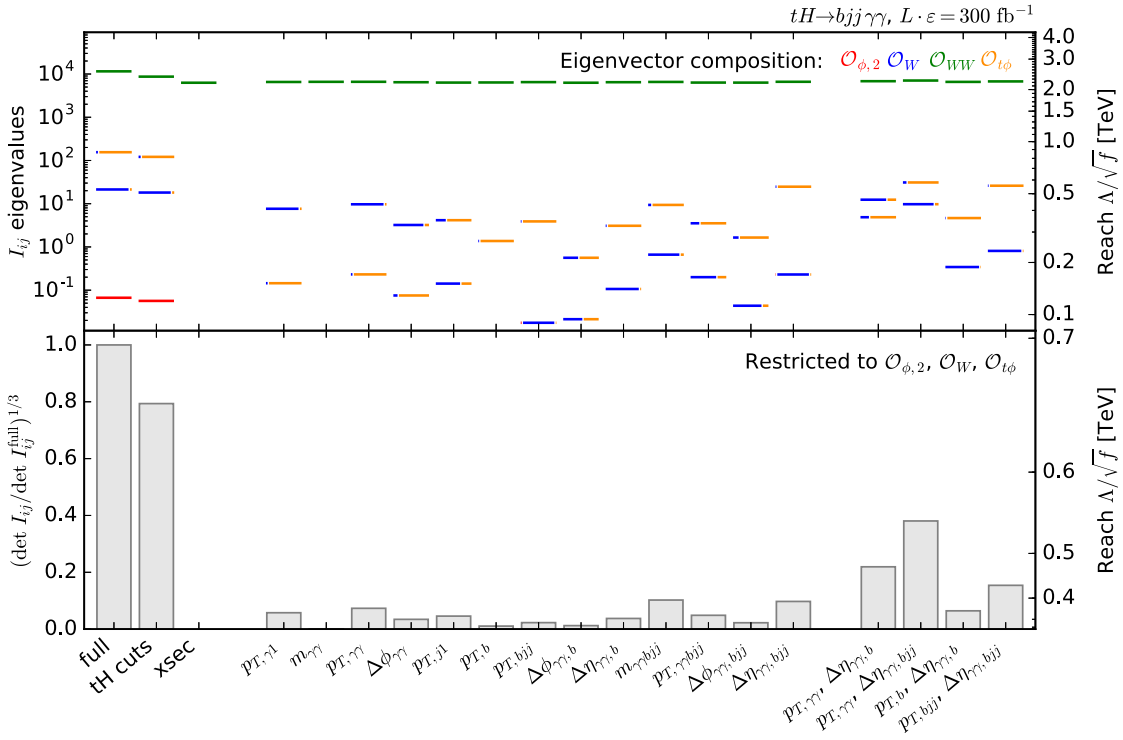

FIG. 15. Fisher information for the Higgs plus single top channel exploiting the full phase space, after the cuts in Eq. (25), and for several kinematic distributions. The top panel shows the eigenvalues, the colors denote the composition of the corresponding eigenvectors. The right axis translates the eigenvalues into a new physics reach for the corresponding combination of Wilson coefficients. In the bottom panel, we show the determinants of the Fisher information restricted to $\mathcal{O}_{\phi,2}$, $\mathcal{O}_W$, and $\mathcal{O}_{t\phi}$, normalized to the full information. Again, the right axis translates them into a new physics reach.

VI. CONCLUSIONS

We have used information geometry to calculate the maximum sensitivity of Higgs measurements to dimension-six operators, to understand the structure of the observables, and to discuss how to improve these measurements. Our approach is based on the Fisher information matrix, which according to the Cramér-Rao bound defines the maximum precision that can be achieved in a measurement. Unlike traditional multivariate analysis techniques, it is designed for continuous, high-dimensional parameter spaces like effective field theories. We have demonstrated how the Fisher information can be reliably calculated using Monte Carlo techniques.

Going beyond global statements, the Fisher information can be studied differentially to understand how the discriminating power is distributed over phase space, which helps guide event selection strategies. Moreover, we can also calculate the information contained in subsets of kinematic distributions. This helps us determine which observables are the most powerful, and allows us to compare the constraining power in conventional analyses with one or two variables to that in more complex multivariate analyses.

Our first testing ground was Higgs production in weak boson fusion with decays into a tau pair or into four leptons. Crucial information comes from the high-energy tails as well as from angular correlations between jets. Decay kinematics hardly adds any information, since the momentum flow is limited by the Higgs mass and gauge invariance forces us to include operators with a momentum dependence. Tight cuts on the rapidity separation of the tagging jets throw away a large amount of discrimination power. Under idealized conditions, conventional analyses based on a simple event selection and standard kinematic distributions can probe new physics scales around 900 GeV in the early phase of run II. Multivariate analyses have the potential to significantly enhance the sensitivity and probe new physics scales of up to 1.2 TeV.

In Higgs production with a single top, we find that kinematic properties of the Higgs decay products and observables in the top system provide orthogonal information. The transverse momenta of the di-photon system as well as the rapidity separation of the $\gamma\gamma$ and bjj systems are powerful observables. But even with HL-LHC data these distributions are only sensitive to new physics scales around 550 GeV, while a multivariate analysis might be able to probe scales up to 700 GeV.

To summarize, information geometry provides a powerful and intuitive tool that can help understand the phenomenology of models with a continuous, high-dimensional parameter space, and in turn can be used to optimize measurement strategies. We have demonstrated this approach in different Higgs channels for dimension-six operators, but it can easily be translated to other processes and models.

ACKNOWLEDGMENTS

We would like to thank Juan Gonzalez-Fraile for many fruitful discussions and sharing his model file for some of the dimension-six operators. We are grateful to Peter Schichtel for helping us to set up and use MadMax. We would also like to acknowledge Ben Allanach's early interest in pursuing information geometry in the context of supersymmetry. J. B. is funded by the DFG through the Graduiertenkolleg, *Particle physics beyond the Standard Model* (GRK 1940). K. C. is supported through National Science Foundation (NSF) Grants No. ACI-1450310 and No. PHY-1505463. The work of F. K. is supported by the NSF under Grant No. PHY-1620638. T. P. is supported by the DFG Forschergruppe, *New Physics at the LHC* (FOR 2239). The authors acknowledge support by the state of Baden-Württemberg through bwHPC.

APPENDIX: ADDITIONAL RESULTS

1. A simple example

As a simple example, we study the Fisher information in a number of rates n_c measured in various Higgs channels c. In the absence of systematic uncertainties, they follow Poisson statistics,

$$f(\mathbf{n}|\boldsymbol{\nu}) = \prod_c \mathrm{Pois}(n_c|\nu_c) = \prod_c \frac{\nu_c^{n_c} e^{-\nu_c}}{n_c!}. \tag{A1}$$

We can calculate the Fisher information in terms of the Poisson mean $\boldsymbol{\nu}$ as

$$\frac{\partial \log f}{\partial \nu_c} = \frac{n_c}{\nu_c} - 1 \quad \frac{\partial^2 \log f}{\partial \nu_c \nu_{c'}} = -\frac{\delta_{cc'} n_c}{\nu_c^2}$$
$$I_{cc'} \equiv -E\left[\frac{\partial^2 \log f}{\partial \nu_c \nu_{c'}}\middle|\boldsymbol{\nu}\right] = \frac{\delta_{cc'}}{\nu_c}. \tag{A2}$$

If we express the expected count rates in terms of model parameters g_i, the Fisher information becomes

$$I_{ij} = \sum_c \frac{1}{\nu_c} \frac{\partial \nu_c}{\partial g_i} \frac{\partial \nu_c}{\partial g_j}. \tag{A3}$$

The matrix $\partial \nu_c / \partial g_i$ is determined by selection requirements, detector acceptance, and efficiencies. In the κ framework, that only scales cross sections and branching ratios, and the matrix $\partial \nu_c / \partial g_i$ is trivial to calculate in closed form. For each channel, this matrix is singular, which means it measures one direction in parameter space and is blind to all others. At least as many channels as parameters are required to make the combined information in Eq. (A3) nonsingular and remove all blind directions (assuming the channels do not provide degenerate information, i. e. the same eigenvectors in the Fisher information).

For illustration, we consider the case where we want to measure one coupling g in one channel with the expected number of events:

$$\nu = L(\sigma_S + \sigma_B) = Lg^2\sigma_0 + L\sigma_B. \tag{A4}$$

The Fisher information is then

$$I = 4L\frac{g^2\sigma_0^2}{g^2\sigma_0 + \sigma_B} = \frac{4L}{g^2}\frac{\sigma_S^2}{\sigma_S + \sigma_B}. \tag{A5}$$

According to the Cramér-Rao bound, the standard deviation of any unbiased estimator $\hat{g}$ is at least

$$\frac{\Delta\hat{g}}{g} \geq \frac{1}{g\sqrt{I}} = \frac{1}{2\sqrt{L}}\frac{\sqrt{\sigma_S + \sigma_B}}{\sigma_S}. \tag{A6}$$

The three terms show how the sensitivity to g profits from the square in the cross section, the square-root dependence on the statistics, and the dependence on the signal-to-background ratio.

2. The MadFisher algorithm

We calculate the Fisher information in Eq. (7) with Monte Carlo methods. With

$$\int dx f^{(1)}(x) \to \sum_{\text{events k}} \Delta\sigma_k/\sigma, \tag{A7}$$

we find

$$I_{ij}(\mathbf{g}) = \sum_{\text{events}k} \frac{L}{\Delta\sigma_k(\mathbf{g})}\frac{\partial\Delta\sigma_k(\mathbf{g})}{\partial g_i}\frac{\partial\Delta\sigma_k(\mathbf{g})}{\partial g_j}, \tag{A8}$$

requiring the differential cross sections and their derivatives as input.

We first generate event samples for a number of benchmark parameters with MadMax [21]. This add-on to MadGraph 5 [26] allows us to simultaneously calculate differential rates

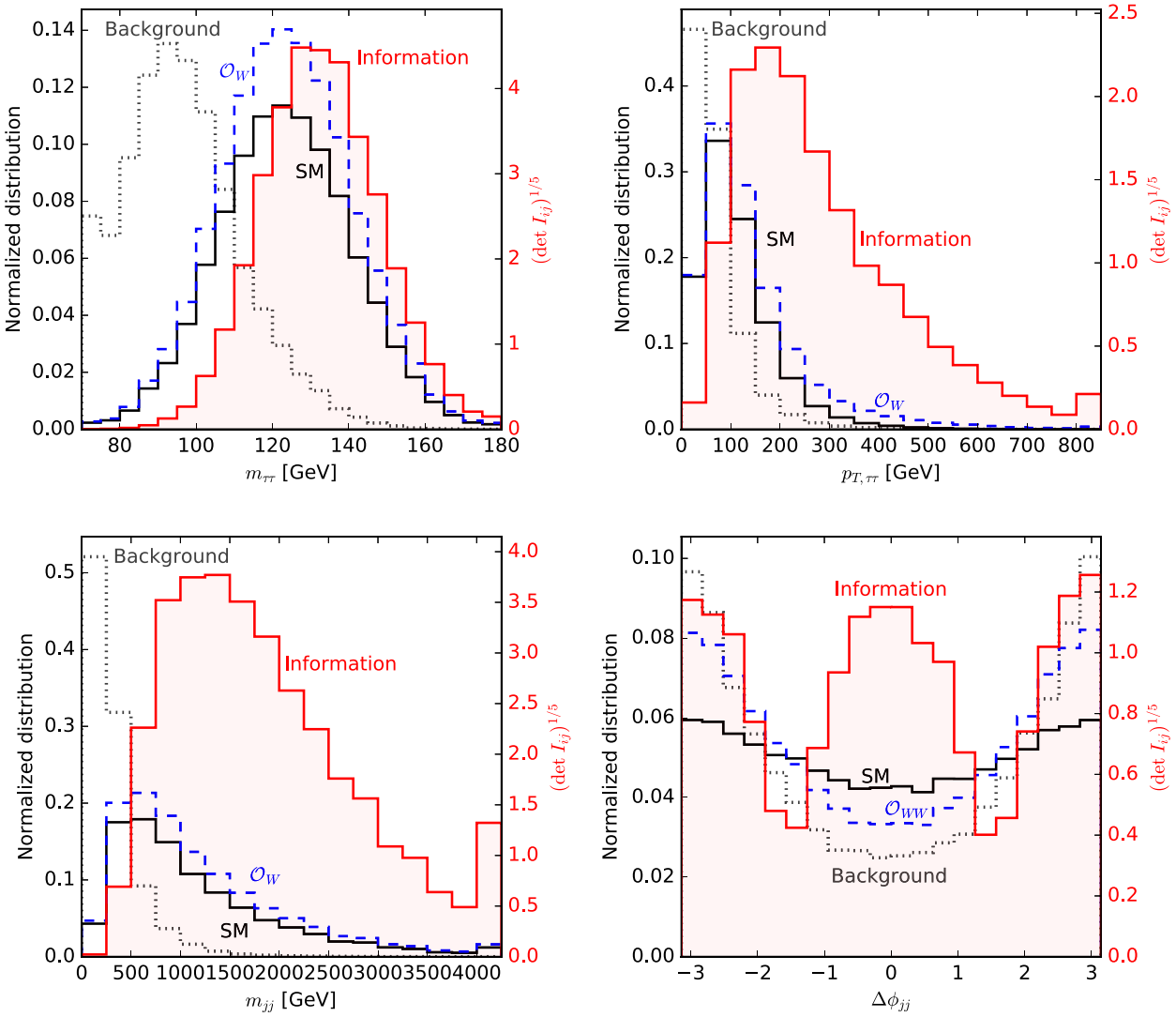

FIG. 16. Distribution of the Fisher information in the WBF $H \to \tau\tau$ channel (shaded red). We also show the normalized SM signal (solid black) and QCD Z + jets (dotted grey) rates. The dashed blue line shows the effect of an exaggerated $f_W v^2/\Lambda^2 = 0.5$ ($f_{WW} v^2/\Lambda^2 = 0.5$ in the bottom right panel). The first (last) bins are underflow (overflow) bins.

for different parameter points using the same phase-space grid. Our FeynRules [30] model file of the relevant dimension-six operators does not truncate operator effects at $\mathcal{O}(1/\Lambda^2)$. MadMax requires fixed renormalization and factorization scales, which we set following Ref. [7]. To keep the calculation times manageable, we restrict some processes to the dominant subprocesses, for instance to initial-state u and d quarks in the WBF case. We then normalize the Higgs rates to the LHC HXS WG recommendations for the total cross section [7], calculating the effect of the different acceptance regions with MadGraph 5. Background processes are simply rescaled to MadGraph predictions.

A morphing technique allows us to calculate the differential cross sections and their derivatives at arbitrary positions in parameter space [31]. The effect of $\mathcal{O}_{\phi,2}$ and systematic rate uncertainties (see Sec. A 4) is taken into account analytically. The contributions from the other operators are decomposed into a number of basis components and can be exactly reconstructed from a set of simulated benchmark points. Our example processes require up to 70 such basis components (in the WBF $H \to 4\ell$ case).

We can then easily calculate the Fisher information according to Eq. (A8). Finally, global distances as in Eq. (5) are calculated in analogy to free fall in general relativity: a starting point and a set of directions in parameter space define the initial conditions, from which we numerically calculate distances along curves defined by the geodesic equation.

3. Additional distributions

In Fig. 16, we show the distribution of the differential information in the WBF $H \to \tau\tau$ channel over various

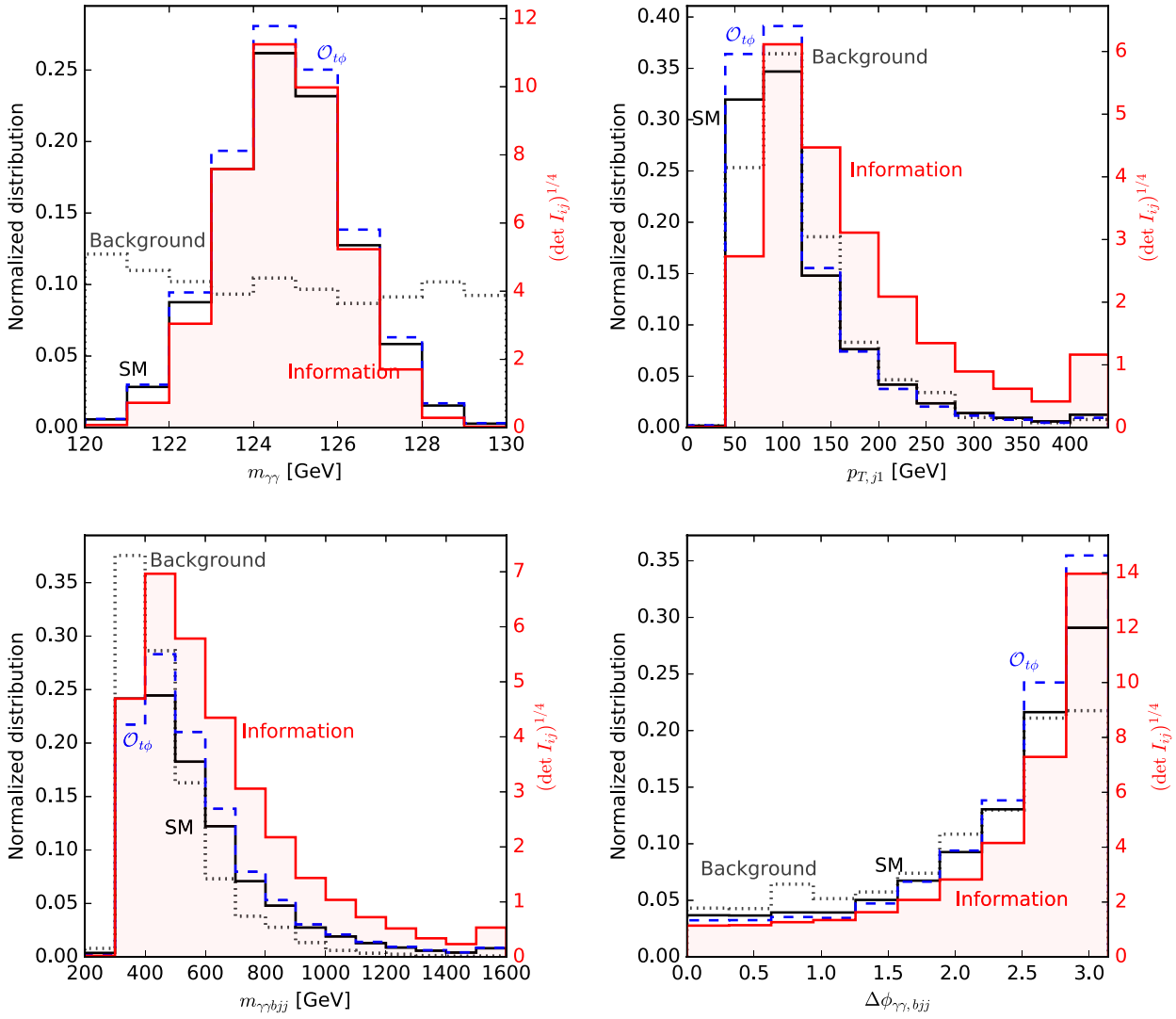

FIG. 17. Distribution of the Fisher information in the Higgs plus single top channel (shaded red). We also show the normalized SM signal (solid black) and single-top background (dotted grey) rates. The dashed blue line shows the effect of $f_{t\phi}v^2/\Lambda^2 = 0.2$. The first (last) bins are underflow (overflow) bins.

kinematic variables. Figure 17 contains similar distributions for the Higgs plus single top channel.

4. Systematic uncertainties

Our information geometry approach can easily be extended to include systematic and theory uncertainties. The parameter space then consists of nuisance parameters ν_i in addition to the Wilson coefficients, and constraint terms are added to the likelihood. If for instance the kth parameter is a nuisance parameter with a Gaussian constraint term with width σ_k, the additional term in the Fisher information reads

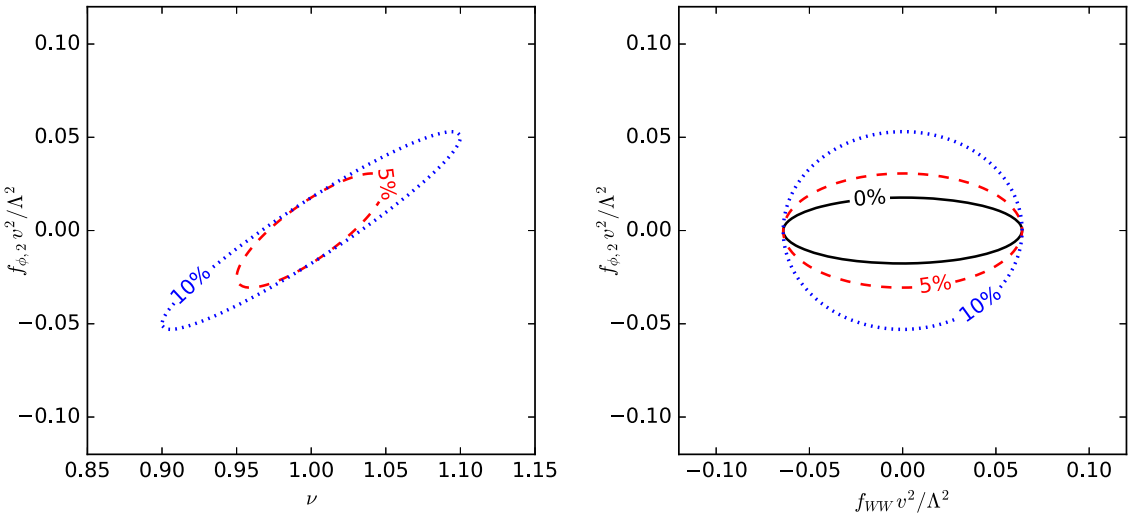

FIG. 18. Effects of Gaussian uncertainties of 5% and 10% on the total signal rate. In the left panel, we show the expected error ellipse $d_{\text{local}}((g,\nu);\mathbf{0}) = 1$ in the plane spanned by a physical parameter and the nuisance parameter ν rescaling the signal rate. In the right panel, we show the error ellipses in the $\mathcal{O}_W - \mathcal{O}_{\phi,2}$ plane after profiling over this systematic uncertainty.

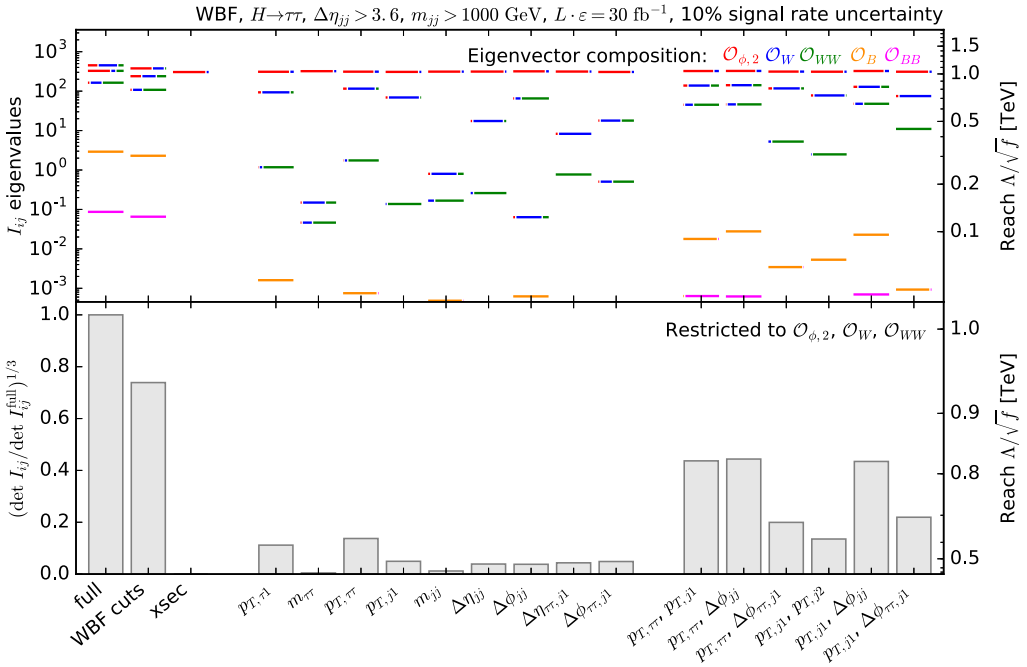

FIG. 19. Fisher information for the WBF $H \to \tau\tau$ channel profiled over a 10% signal rate uncertainty. We compare the information for the full phase space, after the cuts in Eq. (15), and for several kinematic distributions. The top panel shows the eigenvalues, the colors denote the composition of the corresponding eigenvectors. The right axis translates the eigenvalues into a new physics reach for the corresponding combination of Wilson coefficients. In the bottom panel we show the determinants of the Fisher information restricted to $\mathcal{O}_{\phi,2}$, $\mathcal{O}_W$, and $\mathcal{O}_{WW}$, normalized to the full information. Again, the right axis translates them into a new physics reach.

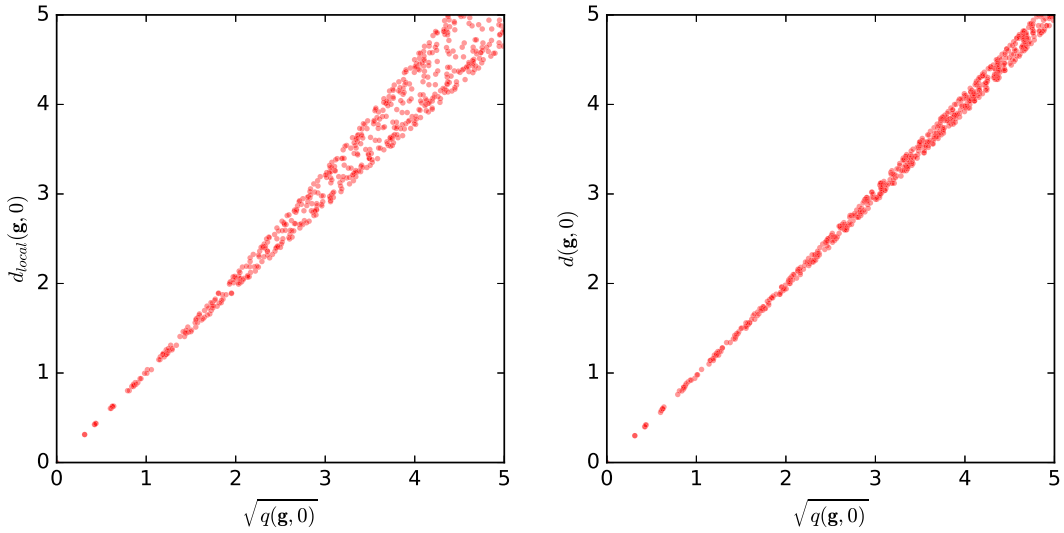

FIG. 20. Comparison of the local (left) and global (right) distances defined by the Fisher information with the expected local likelihood ratio. We use WBF Higgs production in the $\tau\tau$ mode and sample parameter points in the $\mathcal{O}_W - \mathcal{O}_{WW}$ plane.

$$I_{ij}(\mathbf{g},\boldsymbol{\nu}) = \ldots + \frac{\delta_{ik}\delta_{jk}}{\sigma_k^2}. \tag{A9}$$

This also applies to a log-normal constraint through reparametrization of ν. Local and global distances now refer to combined theory and nuisance parameters $(\mathbf{g},\boldsymbol{\nu})$.

We define a profiled local distance between two points $\mathbf{g}_b$ and $\mathbf{g}_a$:

$$d_{\text{profiled}}(\mathbf{g}_b,\mathbf{g}_a) = \min_{\boldsymbol{\nu}} d_{\text{local}}((\mathbf{g}_b,\boldsymbol{\nu});(\mathbf{g}_a,\mathbf{0})). \tag{A10}$$

Equivalently, we can define a profiled Fisher information matrix. Assuming the last parameter to be the only nuisance parameter, the Fisher information matrix has the form

$$I_{ij} = \begin{pmatrix} I^{\text{theory}} & \mathbf{m} \\ \mathbf{m}^T & n \end{pmatrix}, \tag{A11}$$

where I^{theory} is the information matrix restricted to the theory parameters, the vector $\mathbf{m}$ describes the mixing between theory and nuisance parameter, and n is the component that only affects the nuisance parameters. Technically described by the parallel projection of an ellipsoid, the projected Fisher information is given by

$$I_{\text{profiled}\,ij} = I_{ij}^{\text{theory}} - \frac{m_i m_j}{n}. \tag{A12}$$

We demonstrate this for WBF Higgs production in the $\tau\tau$ mode in Fig. 18. We assign a 5% or 10% Gaussian uncertainty on the overall signal rate, representing, for instance, missing higher orders, pdf, or efficiency uncertainties. This significantly reduces the information in the total rate and, thus, mostly the expected precision in the $\mathcal{O}_{\phi,2}$ direction. In Fig. 19, we show how the information in various distributions is affected by such an uncertainty. The new physics reach in the $\mathcal{O}_{\phi,2}$ direction is reduced by 800 GeV.

5. Likelihood ratios and Fisher distance

There is some subtlety in the relationship between standard likelihood ratio tests and the Fisher distance. We anticipate that the confidence intervals in $\mathbf{g}$ will continue to be based on likelihood ratio tests. While both are invariant to reparametrization of $\mathbf{g}$, nonlinear terms in $\mathbf{g}$ that lead to curvature in the information geometry can break the one-to-one relationship between the expected value of the log-likelihood ratio and the Fisher information distance.

In Fig. 20, we compare the two tools. As an example, we study WBF Higgs production in the $\tau\tau$ mode and sample parameter points $\mathbf{g}$ in the $\mathcal{O}_W - \mathcal{O}_{WW}$ plane. For each of these points, we calculate the local and global distance from the SM defined by the Fisher information, as well as the expected log-likelihood ratio:

$$q(\mathbf{g}_b,\mathbf{g}_a) \equiv -2E\left[\log\frac{f(\mathbf{x}|\mathbf{g}_b)}{f(\mathbf{x}|\mathbf{g}_a)}\middle|\mathbf{g}_a\right]. \tag{A13}$$

For small significance deviations, the local and especially the global distances are almost exactly equal to the expected likelihood ratio, with differences only becoming visible around the 3σ level. This demonstrates that different statistical tools probe the same physics and can be chosen based on convenience.

[1] P. W. Higgs, Phys. Lett. **12**, 132 (1964); Phys. Rev. Lett. **13**, 508 (1964); F. Englert and R. Brout, Phys. Rev. Lett. **13**, 321 (1964).

[2] G. Aad *et al.* (ATLAS Collaboration), Phys. Lett. B **716**, 1 (2012); S. Chatrchyan *et al.* (CMS Collaboration), Phys. Lett. B **716**, 30 (2012).

[3] S. Weinberg, Phys. Lett. B **91**, 51 (1980); S. R. Coleman, J. Wess, and B. Zumino, Phys. Rev. **177**, 2239 (1969); C. G. Callan, Jr., S. R. Coleman, J. Wess, and B. Zumino, Phys. Rev. **177**, 2247 (1969).

[4] C. J. C. Burges and H. J. Schnitzer, Nucl. Phys. **B228**, 464 (1983); C. N. Leung, S. T. Love, and S. Rao, Z. Phys. C **31**, 433 (1986); W. Buchmüller and D. Wyler, Nucl. Phys. **B268**, 621 (1986).

[5] For reviews, see e.g. M. S. Bilenky and A. Santamaria, Nucl. Phys. **B420**, 47 (1994); G. Buchalla, A. J. Buras, and M. E. Lautenbacher, Rev. Mod. Phys. **68**, 1125 (1996); C. Englert, A. Freitas, M. M. Mühlleitner, T. Plehn, M. Rauch, M. Spira, and K. Walz, J. Phys. G **41**, 113001 (2014).

[6] For a comprehensive analysis of run I and LEP data and including weak boson production, see e. g. A. Butter, O. J. P. Eboli, J. Gonzalez-Fraile, M. C. Gonzalez-Garcia, T. Plehn, and M. Rauch, J. High Energy Phys. 07 (2016) 152; A. Falkowski, M. Gonzalez-Alonso, A. Greljo, D. Marzocca, and M. Son, arXiv:1609.06312.

[7] D. de Florian *et al.* (LHC Higgs Cross Section Working Group Collaboration), arXiv:1610.07922.

[8] K. Kondo, J. Phys. Soc. Jpn. **57**, 4126 (1988); **60**, 836 (1991); R. H. Dalitz and G. R. Goldstein, Phys. Rev. D **45**, 1531 (1992); D. Atwood and A. Soni, Phys. Rev. D **45**, 2405 (1992); Y. Gao, A. V. Gritsan, Z. Guo, K. Melnikov, M. Schulze, and N. V. Tran, Phys. Rev. D **81**, 075022 (2010); A. V. Gritsan, R. Rntsch, M. Schulze, and M. Xiao, Phys. Rev. D **94**, 055023 (2016); for some recent progress beyond leading order, see e.g. T. Martini and P. Uwer, J. High Energy Phys. 09 (2015) 083.

[9] For a review, see e.g. K. Cranmer, arXiv:1503.07622.

[10] K. Cranmer, J. Pavez, and G. Louppe, arXiv:1506.02169; K. Cranmer and G. Louppe, J. Brief Ideas,.

[11] B. Efron, Annali di statistica **3**, 1189 (1975); S. Amari, *Differential-Geometrical Methods in Statistics* (Springer, New York, 1985).

[12] R. C. Rao, Bull. Calcutta Math. Soc. **37**, 81 (1945); H. Cramér, *Mathematical Methods of Statistics* (Princeton University Press, 1946).

[13] CMS Collaboration, Report No. CMS-PAS-TOP-15-008; for applications in other fields, see for instance P. Jaranowski and A. P. Królak, Phys. Rev. D **49**, 1723 (1994).

[14] J. Neyman and E. S. Pearson, Phil. Trans. R. Soc. A **231**, 289 (1933).

[15] K. Cranmer and T. Plehn, Eur. Phys. J. C **51**, 415 (2007).

[16] D. Rainwater, arXiv:hep-ph/0702124; M. Rauch, arXiv: 1610.08420.

[17] R. Kleiss and W. J. Stirling, Phys. Lett. B **200**, 193 (1988); U. Baur and E. W. N. Glover, Phys. Lett. B **252**, 683 (1990); V. D. Barger, K. m. Cheung, T. Han, J. Ohnemus, and D. Zeppenfeld, Phys. Rev. D **44**, 1426 (1991); D. L. Rainwater, R. Szalapski, and D. Zeppenfeld, Phys. Rev. D **54**, 6680 (1996); B. E. Cox, J. R. Forshaw, and A. D. Pilkington, Phys. Lett. B **696**, 87 (2011); E. Gerwick, T. Plehn, and S. Schumann, Phys. Rev. Lett. **108**, 032003 (2012).

[18] T. Plehn, D. L. Rainwater, and D. Zeppenfeld, Phys. Rev. Lett. **88**, 051801 (2002); K. Hagiwara, Q. Li, and K. Mawatari, J. High Energy Phys. 07 (2009) 101; C. Englert, D. Goncalves-Netto, K. Mawatari, and T. Plehn, J. High Energy Phys. 01 (2013) 148; C. Englert, D. Goncalves, G. Nail, and M. Spannowsky, Phys. Rev. D **88**, 013016 (2013); K. Hagiwara and S. Mukhopadhyay, J. High Energy Phys. 05 (2013) 019; M. R. Buckley, T. Plehn, and M. J. Ramsey-Musolf, Phys. Rev. D **90**, 014046 (2014); arXiv:1403.2726; J. Brehmer, J. Jaeckel, and T. Plehn, Phys. Rev. D **90**, 054023 (2014); A. Greljo, G. Isidori, J. M. Lindert, and D. Marzocca, Eur. Phys. J. C **76**, 158 (2016).

[19] D. Rainwater, D. Zeppenfeld, and K. Hagiwara, Phys. Rev. D **59**, 014037 (1998); T. Plehn, D. L. Rainwater, and D. Zeppenfeld, Phys. Rev. D **61**, 093005 (2000).

[20] F. Maltoni, K. Paul, T. Stelzer, and S. Willenbrock, Phys. Rev. D **64**, 094023 (2001); S. Biswas, E. Gabrielli, and B. Mele, J. High Energy Phys. 01 (2013) 088; M. Farina, C. Grojean, F. Maltoni, E. Salvioni, and A. Thamm, J. High Energy Phys. 05 (2013) 022; C. Englert and E. Re, Phys. Rev. D **89**, 073020 (2014); F. Demartin, F. Maltoni, K. Mawatari, and M. Zaro, Eur. Phys. J. C **75**, 267 (2015).

[21] T. Plehn, P. Schichtel, and D. Wiegand, Phys. Rev. D **89**, 054002 (2014); F. Kling, T. Plehn, and P. Schichtel, arXiv: 1607.07441.

[22] J. Brehmer, A. Freitas, D. Lopez-Val, and T. Plehn, Phys. Rev. D **93**, 075014 (2016); A. Biekötter, J. Brehmer, and T. Plehn, Phys. Rev. D **94**, 055032 (2016).

[23] G. Aad *et al.* (ATLAS Collaboration), J. High Energy Phys. 04 (2015) 117.

[24] K. Hagiwara, S. Ishihara, R. Szalapski, and D. Zeppenfeld, Phys. Rev. D **48**, 2182 (1993).

[25] T. Corbett, O. J. P. Eboli, J. Gonzalez-Fraile, and M. C. Gonzalez-Garcia, Phys. Rev. D **87**, 015022 (2013).

[26] J. Alwall, R. Frederix, S. Frixione, V. Hirschi, F. Maltoni, O. Mattelaer, H.-S. Shao, T. Stelzer, P. Torrielli, and M. Zaro, J. High Energy Phys. 07 (2014) 079.

[27] G. Klamke and D. Zeppenfeld, J. High Energy Phys. 04 (2007) 052.

[28] F. Kling, T. Plehn, and M. Takeuchi, Phys. Rev. D **86**, 094029 (2012).

[29] CMS Collaboration, Report No. CMS-PAS-HIG-15-005.

[30] A. Alloul, N. D. Christensen, C. Degrande, C. Duhr, and B. Fuks, Comput. Phys. Commun. **185**, 2250 (2014).

[31] ATLAS Collaboration, Report No. ATL-PHYS-PUB-2015-047, 2015, http://cds.cern.ch/record/2066980.